

# Discovery of VHE emission towards the Carina arm region with the H.E.S.S. telescope array: HESS J1018–589

HESS Collaboration, A. Abramowski<sup>1</sup>, F. Acero<sup>2</sup>, F. Aharonian<sup>3,4,5</sup>, A.G. Akhperjanian<sup>6,5</sup>, G. Anton<sup>7</sup>, A. Balzer<sup>7</sup>, A. Barnacka<sup>8,9</sup>, Y. Becherini<sup>10,11</sup>, J. Becker<sup>12</sup>, K. Bernlöhr<sup>3,13</sup>, E. Birsin<sup>13</sup>, J. Biteau<sup>11</sup>, A. Bochow<sup>3</sup>, C. Boisson<sup>14</sup>, J. Bolmont<sup>15</sup>, P. Bordas<sup>16</sup>, J. Brucker<sup>7</sup>, F. Brun<sup>11</sup>, P. Brun<sup>9</sup>, T. Bulik<sup>17</sup>, I. Büsching<sup>18,12</sup>, S. Carrigan<sup>3</sup>, S. Casanova<sup>18,3</sup>, M. Cerruti<sup>14</sup>, P.M. Chadwick<sup>19</sup>, A. Charbonnier<sup>15</sup>, R.C.G. Chaves<sup>9,3</sup>, A. Cheesbrough<sup>19</sup>, G. Cologna<sup>20</sup>, J. Conrad<sup>21</sup>, M. Dalton<sup>13</sup>, M.K. Daniel<sup>19</sup>, I.D. Davids<sup>22</sup>, B. Degrange<sup>11</sup>, C. Deil<sup>3</sup>, H.J. Dickinson<sup>21</sup>, A. Djannati-Ataï<sup>10</sup>, W. Domainko<sup>3</sup>, L.O'C. Drury<sup>4</sup>, G. Dubus<sup>23</sup>, K. Dutson<sup>24</sup>, J. Dyks<sup>8</sup>, M. Dyrda<sup>25</sup>, K. Egberts<sup>26</sup>, P. Eger<sup>7</sup>, P. Espigat<sup>10</sup>, L. Fallon<sup>4</sup>, S. Fegan<sup>11</sup>, F. Feinstein<sup>2</sup>, M.V. Fernandes<sup>1</sup>, A. Fiasson<sup>27</sup>, G. Fontaine<sup>11</sup>, A. Förster<sup>3</sup>, M. Füßling<sup>13</sup>, Y.A. Gallant<sup>2</sup>, H. Gast<sup>3</sup>, L. Gérard<sup>10</sup>, D. Gerbig<sup>12</sup>, B. Giebels<sup>11</sup>, J.F. Glicenstein<sup>9</sup>, B. Glück<sup>7</sup>, D. Göring<sup>7</sup>, S. Häffner<sup>7</sup>, J.D. Hague<sup>3</sup>, J. Hahn<sup>3</sup>, D. Hampf<sup>1</sup>, J. Harris<sup>19</sup>, M. Hauser<sup>20</sup>, S. Heinz<sup>7</sup>, G. Heinzelmann<sup>1</sup>, G. Henri<sup>23</sup>, G. Hermann<sup>3</sup>, A. Hillert<sup>3</sup>, J.A. Hinton<sup>24</sup>, W. Hofmann<sup>3</sup>, P. Hofverberg<sup>3</sup>, M. Holler<sup>7</sup>, D. Horns<sup>1</sup>, A. Jacholkowska<sup>15</sup>, O.C. de Jager<sup>18</sup>, C. Jahn<sup>7</sup>, M. Jamrozy<sup>28</sup>, I. Jung<sup>7</sup>, M.A. Kastendieck<sup>1</sup>, K. Katarzyński<sup>29</sup>, U. Katz<sup>7</sup>, S. Kaufmann<sup>20</sup>, D. Keogh<sup>19</sup>, B. Khélifi<sup>11</sup>, D. Klochokov<sup>16</sup>, W. Kluźniak<sup>8</sup>, T. Kneiske<sup>1</sup>, Nu. Komin<sup>27</sup>, K. Kosack<sup>9</sup>, R. Kossakowski<sup>27</sup>, F. Krayzel<sup>27</sup>, H. Laffon<sup>11</sup>, G. Lamanna<sup>27</sup>, J.-P. Lenain<sup>20</sup>, D. Lennarz<sup>3</sup>, T. Lohse<sup>13</sup>, A. Lopatin<sup>7</sup>, C.-C. Lu<sup>3</sup>, V. Marandon<sup>3</sup>, A. Marcowith<sup>2</sup>, J. Masbou<sup>27</sup>, N. Maxted<sup>30</sup>, M. Mayer<sup>7</sup>, T.J.L. McComb<sup>19</sup>, M.C. Medina<sup>9</sup>, J. Méhault<sup>2</sup>, R. Moderski<sup>8</sup>, M. Mohamed<sup>20</sup>, E. Moulin<sup>9</sup>, C.L. Naumann<sup>15</sup>, M. Naumann-Godo<sup>9</sup>, M. de Naurois<sup>11</sup>, D. Nedbal<sup>31</sup>, D. Nekrasov<sup>3</sup>, N. Nguyen<sup>1</sup>, B. Nicholas<sup>30</sup>, J. Niemiec<sup>25</sup>, S.J. Nolan<sup>19</sup>, S. Ohm<sup>32,24,3</sup>, E. de Oña Wilhelmi<sup>3</sup>, B. Opitz<sup>1</sup>, M. Ostrowski<sup>28</sup>, I. Oya<sup>13</sup>, M. Panter<sup>3</sup>, M. Paz Arribas<sup>13</sup>, N.W. Pekeur<sup>18</sup>, G. Pelletier<sup>23</sup>, J. Perez<sup>26</sup>, P.-O. Petrucci<sup>23</sup>, B. Peyaud<sup>9</sup>, S. Pita<sup>10</sup>, G. Pühlhofer<sup>16</sup>, M. Punch<sup>10</sup>, A. Quirrenbach<sup>20</sup>, M. Raue<sup>1</sup>, S.M. Rayner<sup>19</sup>, A. Reimer<sup>26</sup>, O. Reimer<sup>26</sup>, M. Renaud<sup>2</sup>, R. de los Reyes<sup>3</sup>, F. Rieger<sup>3,33</sup>, J. Ripken<sup>21</sup>, L. Rob<sup>31</sup>, S. Rosier-Lees<sup>27</sup>, G. Rowell<sup>30</sup>, B. Rudak<sup>8</sup>, C.B. Rulten<sup>19</sup>, V. Sahakian<sup>6,5</sup>, D.A. Sanchez<sup>3</sup>, A. Santangelo<sup>16</sup>, R. Schlickeiser<sup>12</sup>, A. Schulz<sup>7</sup>, U. Schwanke<sup>13</sup>, S. Schwarzburg<sup>16</sup>, S. Schwemmer<sup>20</sup>, F. Sheidaei<sup>10,18</sup>, J.L. Skilton<sup>3</sup>, H. Sol<sup>14</sup>, G. Spengler<sup>13</sup>, L. Stawarz<sup>28</sup>, R. Steenkamp<sup>22</sup>, C. Stegmann<sup>7</sup>, F. Stinzing<sup>7</sup>, K. Stycz<sup>7</sup>, I. Sushch<sup>13\*</sup>, A. Szostek<sup>28</sup>, J.-P. Tavernet<sup>15</sup>, R. Terrier<sup>10</sup>, M. Tluczykont<sup>1</sup>, K. Valerius<sup>7</sup>, C. van Eldik<sup>7,3</sup>, G. Vasileiadis<sup>2</sup>, C. Venter<sup>18</sup>, A. Viana<sup>9</sup>, P. Vincent<sup>15</sup>, H.J. Völk<sup>3</sup>, F. Volpe<sup>3</sup>, S. Vorobiov<sup>2</sup>, M. Vorster<sup>18</sup>, S.J. Wagner<sup>20</sup>, M. Ward<sup>19</sup>, R. White<sup>24</sup>, A. Wierzcholska<sup>28</sup>, M. Zacharias<sup>12</sup>, A. Zajczyk<sup>8,2</sup>, A.A. Zdziarski<sup>8</sup>, A. Zech<sup>14</sup>, and H.-S. Zechlin<sup>1</sup>

(Affiliations can be found after the references)

Received ; accepted

## ABSTRACT

The Carina arm region, containing the supernova remnant SNR G284.3–1.8, the high-energy (HE;  $E > 100$  MeV) binary 1FGL J1018.6–5856 and the energetic pulsar PSR J1016–5857 and its nebula, has been observed with the H.E.S.S. telescope array. The observational coverage of the region in very-high-energy (VHE;  $E > 0.1$  TeV)  $\gamma$ -rays benefits from deep exposure (40 h) of the neighboring open cluster Westerlund 2. The observations have revealed a new extended region of VHE  $\gamma$ -ray emission. The new VHE source HESS J1018–589 shows a bright, point-like emission region positionally coincident with SNR G284.3–1.8 and 1FGL J1018.6–5856 and a diffuse extension towards the direction of PSR J1016–5857. A soft ( $\Gamma = 2.7 \pm 0.5_{\text{stat}}$ ) photon index, with a differential flux at 1 TeV of  $N_0 = (4.2 \pm 1.1) \cdot 10^{-13} \text{ TeV}^{-1} \text{ cm}^{-2} \text{ s}^{-1}$  is found for the point-like source, whereas the total emission region including the diffuse emission region is well fit by a power-law function with spectral index  $\Gamma = 2.9 \pm 0.4_{\text{stat}}$  and differential flux at 1 TeV of  $N_0 = (6.8 \pm 1.6) \cdot 10^{-13} \text{ TeV}^{-1} \text{ cm}^{-2} \text{ s}^{-1}$ . This H.E.S.S. detection motivated follow-up X-ray observations with the XMM-Newton satellite to investigate the origin of the VHE emission. The analysis of the XMM-Newton data resulted in the discovery of a bright, non-thermal point-like source (XMMU J101855.4–58564) with a photon index of  $\Gamma = 1.65 \pm 0.08$  in the center of SNR G284.3–1.8, and a thermal, extended emission region coincident with its bright northern filament. The characteristics of this thermal emission are used to estimate the plasma density in the region as  $n \approx 0.5 \text{ cm}^{-3}$  ( $2.9 \text{ kpc/d}$ )<sup>2</sup>. The position of XMMU J101855.4–58564 is compatible with the position reported by the Fermi-LAT collaboration for the binary system 1FGL J1018.6–5856 and the variable Swift XRT source identified with it. The new X-ray data are used alongside archival multi-wavelength data to investigate the relationship between the VHE  $\gamma$ -ray emission from HESS J1018–589 and the various potential counterparts in the Carina arm region.

**Key words.** gamma-ray: observations; ISM: individual objects: SNR G284.3–1.8, 1FGL J1018.6–5856, PSR J1016–5857

## 1. Introduction

The H.E.S.S. (High Energy Stereoscopic System) collaboration has carried out observations of the Carina arm as part of the Galactic Plane Survey (Aharonian et al. 2006c, 2008a; Gast et al. 2011). The observed region includes three potential VHE  $\gamma$ -ray emitters, SNR G284.3–1.8 (MSH 10–53), the high spin-down luminosity pulsar PSR J1016–5857 (Camilo et al. 2001) and the Fermi-LAT  $\gamma$ -ray binary 1FGL J1018.6–5856 (Abdo et al. 2010). SNR G284.3–1.8 has an incomplete radio shell (Fig. 1) with a non-thermal radio spectrum and a flux density of  $(5.4 \pm 0.8)$  Jy at 8.4 GHz (Milne et al. 1989). Evidence of interaction with molecular clouds (MC;  $^{12}\text{CO}$  J=1–0) has been reported by Ruiz & May (1986) using observations with the 1.2 m Columbia Millimeter-Wave Telescope. The MC content integrated over velocities in the local standard of rest from  $-14.95 \text{ km s}^{-1}$  to  $-21.45 \text{ km s}^{-1}$  traces the radio shell shape of the SNR.

The shell-like SNR shows a bright, narrow filament, co-incident with an  $\text{H}\alpha$  filament (Van der Bergh et al. 1973) to the East. Optical and CO observations imply that SNR G284.3–1.8 is most likely a  $10^4$  yr old remnant of a type II supernova with a massive stellar progenitor and that it is located at a distance of  $d_{\text{SNR}}=2.9 \text{ kpc}$  (with an error of  $\pm 20\%$ ) (Ruiz & May 1986). The western edge of the shell shows a so-called *finger* emission region (see Fig. 1) extended towards the direction of PSR J1016–5857. This Vela-like pulsar and its associated X-ray pulsar wind nebula (PWN), located  $\approx 35'$  away from the geometrical center of the SNR, were discovered by Camilo et al. (2001, 2004) in a search for counterparts of the unidentified source 3EG J1013–5915 (Hartman et al. 1999) with the Parkes telescope. The energetic pulsar, formerly associated with the SNR G284.3–1.8, has a rotation period of 107 ms, a characteristic age  $\tau_c=21 \text{ kyr}$  and a spin-down luminosity of  $2.6 \cdot 10^{36} \text{ erg s}^{-1}$ . Its distance can be estimated from the pulsar’s dispersion measure to be  $d_{\text{PSR}}=9_{-2}^{+3} \text{ kpc}$  (Taylor & Cordes 1993) or  $d_{\text{PSR}} \approx 8 \text{ kpc}$  (Cordes & Lazio 2002). Later observations with *Chandra* (Camilo et al. 2004) resulted in the detection of the associated X-ray PWN, apparently located at the tip of the finger of the SNR radio emission. The PWN spectrum is well fit by a power-law model with photon index  $\Gamma_X=1.32 \pm 0.25$ , absorbing neutral hydrogen column density  $N_{\text{H}}=(5.0 \pm 1.7) \cdot 10^{21} \text{ cm}^{-2}$ , and unabsorbed flux  $F_{0.8-7 \text{ keV}}=2.8 \cdot 10^{-13} \text{ erg cm}^{-2} \text{ s}^{-1}$ . The good match in both width and position angle of the PWN and the SNR finger suggests a possible connection between the two. However, the association of PSR J1016–5857 with SNR G284.3–1.8 is questioned by the large difference in their distance measurements and the large offset between the center of the shell and the pulsar position. Camilo et al. (2004) argue that the uncertainties in the model for the free distribution of electrons in the Galaxy are large along spiral arm tangents, affecting the estimation of the distance inferred from the dispersion measure. A proper motion velocity of  $v_{\text{PSR}}=500 \cdot (d/3 \text{ kpc})(21 \text{ kyr}/\tau_c) \text{ km s}^{-1}$  has to be invoked to connect the pulsar with the geometric center

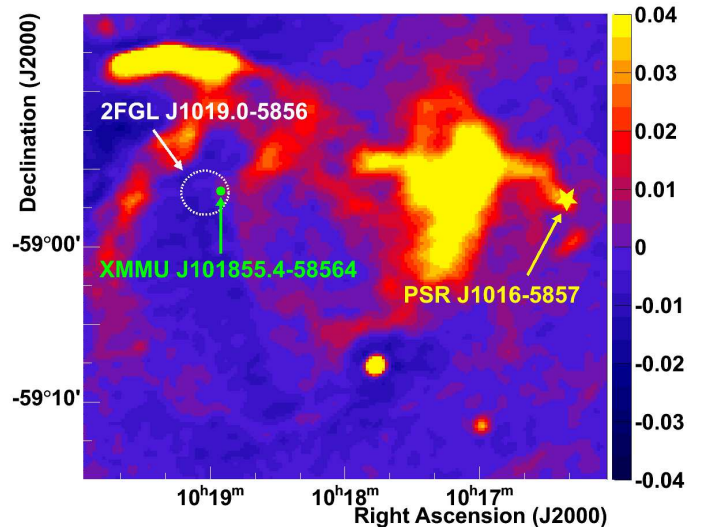


**Fig. 1.** The MOST–Molonglo radio map (in units of Jy/beam) of SNR G284.3–1.8 is displayed together with the position of the Fermi-LAT source 2FGL J1019.0–5856 (white dashed line showing the 95% uncertainty in its position) and its associated X-ray source (green dot, XMMU J101855.4–58564). To the west of the SNR the radio finger is visible extending toward the direction of PSR J1016–5857 (marked with a yellow filled star). The PSF size of the radio image is  $45'' \times 52.5''$ .

of the SNR. Even if the proper motion velocity is within the range of known pulsar velocities, this highly supersonic movement in the local interstellar medium (ISM) would create a bow shock nebula, which has not been observed.

The Fermi-LAT collaboration has reported the detection of a new source 1FGL J1018.6–5856 (or 2FGL J1019.0–5856), positionally coincident with SNR G284.3–1.8 and associated with the EGRET source 3EG J1013–5915 (Abdo et al. 2010, 2011). The source reported in the LAT second-year source catalog shows an energy flux of  $(3.53 \pm 0.11) \cdot 10^{-10} \text{ erg cm}^{-2} \text{ s}^{-1}$  in the 100 MeV to 100 GeV energy band, and a fit to a power-law spectrum yields a photon index of  $\Gamma_{\text{HE}}=2.59 \pm 0.04$ . The AGILE collaboration also reported HE emission from this region and pulsed emission is marginally detected ( $4.8\sigma$ ) from the direction of PSR J1016–5857 (Pellizzonni et al. 2009). The  $\gamma$ -ray emission from 1FGL J1018.6–5856, however, shows a periodic modulation with a period of  $16.58 \pm 0.02$  days, detected by Fermi-LAT (Corbet et al. 2011; Ackermann et al. 2012). This periodicity is taken as evidence that 1FGL J1018.6–5856 is a new  $\gamma$ -ray binary system, with an O6V((f))-type star (2MASS 10185560–5856459) proposed as the stellar counterpart. The spectrum of the periodic source exhibits a break at  $\approx 1 \text{ GeV}$  with best-fit values of  $\Gamma_{\text{HE}}(0.1-1 \text{ GeV})=2.00 \pm 0.04$  and  $\Gamma_{\text{HE}}(1-10 \text{ GeV})=3.09 \pm 0.06$  and an integral energy flux above 100 MeV of  $(2.8 \pm 0.1) \cdot 10^{-10} \text{ erg cm}^{-2} \text{ s}^{-1}$ . The binary nature of the HE source is strengthened by the detection of a periodic X-ray (Swift XRT) and radio (Australia Telescope Compact Array) compact source coincident with the  $\gamma$ -ray source. A counterpart in hard X-rays has also been detected using INTEGRAL data (Li et al. 2011).

Send offprint requests to:

emma@mpi-hd.mpg.de

rterrier@apc.univ-paris7.fr

\* supported by Erasmus Mundus, External Cooperation Window

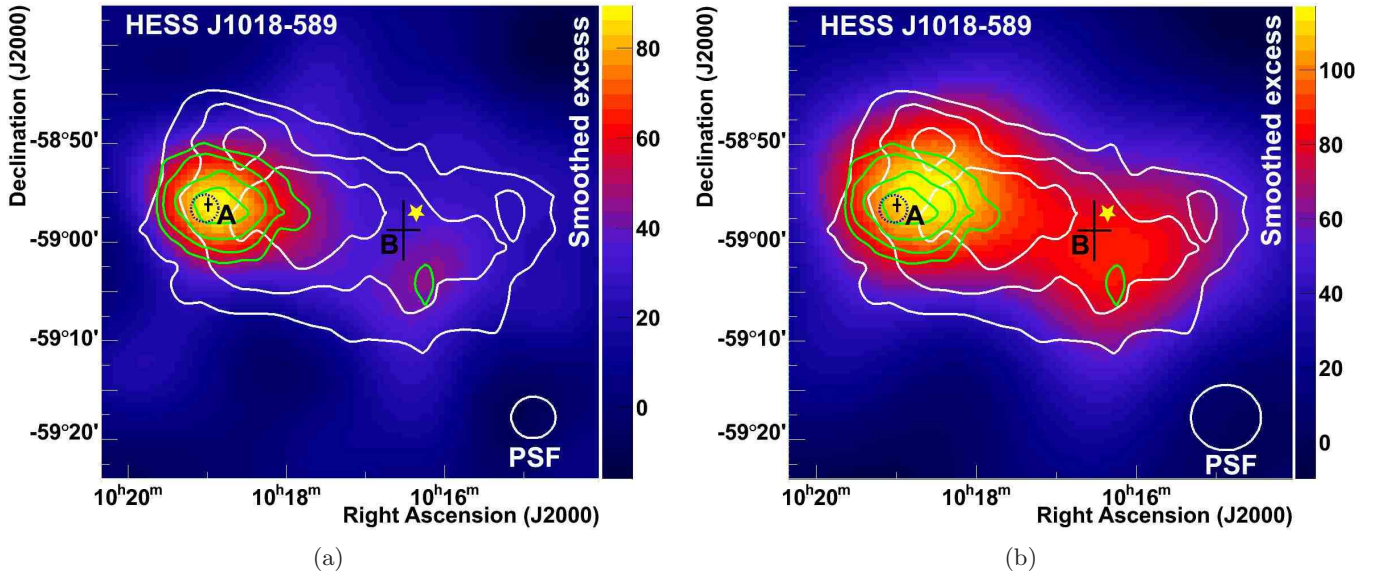


**Fig. 2.** H.E.S.S. excess image of the HESS J1018–589 region smoothed with a Gaussian of width  $\sigma=0.07^\circ$  (on the left, a) and  $\sigma=0.11^\circ$  (on the right, b)). Significance contours, calculated using an oversampling radius of  $0.1^\circ$  (in green) and  $0.22^\circ$  (in white) are shown, starting at  $4\sigma$  in steps of  $1\sigma$ . The black crosses (A and B) mark the best-fit position and statistical errors at  $1\sigma$  level for the two emission regions (see text for details). The position of 1FGL J1018.6–5856 is shown with a blue dashed ellipse (95% confidence level) while the position of PSR J1016–5857 is marked with a yellow star. The white circles illustrate the size of the (68% containment radius) PSF smoothed with the two different Gaussian widths used.

## 2. H.E.S.S. observations

H.E.S.S. is an array of four VHE  $\gamma$ -ray imaging atmospheric Cherenkov telescopes (IACTs) located in the Khomas Highland of Namibia ( $23^\circ16'18''$  S,  $16^\circ30'00''$  E). Each of these telescopes is equipped with a tessellated spherical mirror of  $107\text{ m}^2$  area and a camera comprised of 960 photomultiplier tubes, covering a large field-of-view (FoV) of  $5^\circ$  diameter. The system works in a coincidence mode (see e.g. Funk et al. 2004), requiring at least two of the four telescopes to trigger the detection of an extended air shower (EAS). This stereoscopic approach results in a high angular resolution of  $\approx 6'$  per event, good energy resolution (15% on average) and an efficient background rejection (Aharonian et al. 2006b). The mean (energy-dependent) point spread function (PSF) is estimated to be  $\approx 0.1^\circ$ . These characteristics allow H.E.S.S. to reach a sensitivity of  $\approx 2.0 \cdot 10^{-13}\text{ ph cm}^{-2}\text{ s}^{-1}$  (equivalent to 1% of the Crab Nebula flux above 1 TeV), or better if advanced techniques are used for image analysis (Acero et al. 2009), for a point-like source detected at a significance of  $5\sigma$  in 25 hours of observation at zenith.

The Carina arm region benefits from deep H.E.S.S. observations of the Westerlund 2 region (Abramowski et al. 2010) and an acceptance-corrected effective exposure time of 40 h was obtained towards the direction of SNR G284.3–1.8 and PSR J1016–5857 in a multi-year observation campaign in January and March 2007, April and May 2008, and May to June 2009. The data set consists of scan-mode observations and dedicated observations in wobble-mode, in which the telescopes are pointed offset from the nominal source location to allow simultaneous background estimation (with an offset range in the total data set from  $0.5^\circ$

to  $2.6^\circ$ ). The observations were performed in a zenith angle range from  $35^\circ$  to  $50^\circ$  and the optical response of the system was estimated from the Cherenkov light of single muons as explained in Aharonian et al. (2006b).

The data have been analyzed using a multivariate analysis (Becherini et al. 2011) and cross-checked with the Hillas second moment (Hillas 1984) event reconstruction scheme (Aharonian et al. 2006b) and Model Analysis (de Naurois & Rolland 2009), including independent calibration of pixel amplitudes and identification of problematic or dead pixels in the IACTs cameras, leading to compatible results. To study the morphology of the source with sufficient statistics, a cut of 80 photoelectrons (p.e.) on the intensity of the EAS is used to reduce the data and produce the images, light curve and spectrum of the source. The energy threshold of the analysis presented here is  $E_{\text{th}} \approx 0.6\text{ TeV}$ .

Figure 2 a) shows an image of HESS J1018–589 smoothed with a Gaussian of width  $\sigma=0.07^\circ$ . The background in each pixel is estimated with the ring background method (Aharonian et al. 2006b). This image shows a point-like  $\gamma$ -ray excess centered on the position of 1FGL J1018.6–5856 and SNR G284.3–1.8, and a diffuse emission region extending in the direction of PSR J1016–5857. A peak pre-trials significance of  $8.3\sigma$  (which corresponds to over 6 sigma post-trials) is obtained using an oversampling radius of  $0.10^\circ$  (green contours in Fig. 2). Fig. 2 b) shows the same image but smoothed using a Gaussian of width  $\sigma=0.11^\circ$  to match the significance contours calculated with an oversampling radius of  $0.22^\circ$  (optimized for extended sources, Aharonian et al. 2006c), which are overlaid in white. An extension of the VHE emission towards the West is observed when using the larger radius. The white

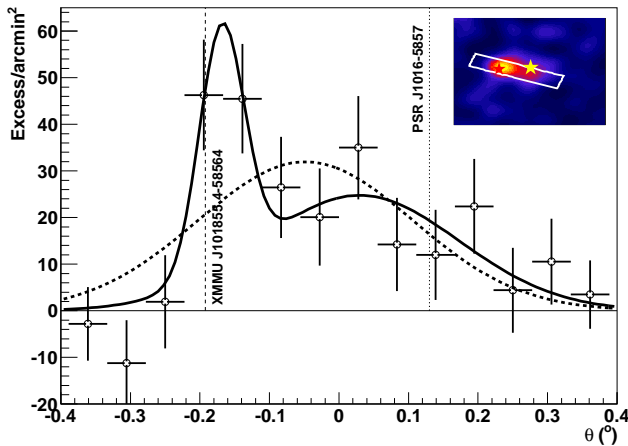


**Fig. 3.** Profile of the VHE emission along the line between the peak of the point-like emission and the peak of the diffuse emission, as illustrated in the inset. Fits using a single and a double Gaussian function are shown in dashed and solid lines respectively. The positions of XMMU J101855.4–58564 and PSR J1016–5857 are marked with dashed and dotted vertical lines and red and yellow stars in the inset, in which the significance image obtained using an oversampling radius of  $0.1^\circ$  is shown.

circles in Fig. 2 illustrate the size of the PSF smoothed with the two different Gaussian widths used.

To investigate the morphology of HESS J1018–589 different models were fit to the uncorrelated excess map using the Sherpa fitting package (Refsdal et al. 2009). The maximum-likelihood-ratio (MLR) test, performed using a Gaussian-shape function convolved with the H.E.S.S. PSF, finds a point-like source at  $\alpha=10^{\text{h}}18^{\text{m}}59.3^{\text{s}}\pm 2.4^{\text{s}}_{\text{stat}}$  and  $\delta=-58^\circ 56' 10''\pm 36''_{\text{stat}}$  (J2000), marked in black in Fig. 2 (position A). The systematic error is estimated to be  $20''$  per axis (Gillissen 2004). Including a second source in the MLR-test results in an improvement of the test statistics by 29.8 (or  $\approx 4.4\sigma$  for a four degree of freedom  $\chi^2$ -test). The best-fit position of the second source (position B) is located at  $\alpha=10^{\text{h}}16^{\text{m}}31^{\text{s}}\pm 12^{\text{s}}_{\text{stat}}$  and  $\delta=-58^\circ 58' 48''\pm 3'_{\text{stat}}$  (J2000) with an extent of  $\sigma=0.15^\circ\pm 0.03^\circ_{\text{stat}}$ .

The two-emission-regions hypothesis is strengthened when the projection of a rectangular region on the uncorrelated excess map along the extension of the image (with a width of twice the H.E.S.S. mean PSF) is evaluated. The fit of a single Gaussian function to the projection yields a  $\chi^2/\nu$  of 21.04/13 (null hypothesis probability  $P=0.072$ ) whereas the fit to a double Gaussian function leads to a better  $\chi^2/\nu$  of 9.6/10 ( $P=0.476$ ). Fig. 3 shows the profile of the rectangular region (in white in the inset). The single and double Gaussian function fits are shown in dashed and solid lines, respectively.

The energy spectrum (shown in Fig. 4) for the VHE excess was computed by means of a forward-folding maximum likelihood fit (Piron et al. 2001). To estimate the background the reflected background method was used, in which symmetric regions, not contaminated by known sources, are used to extract the background (Aharonian et al. 2006b). To derive the source spectrum two regions were selected, one around the point-

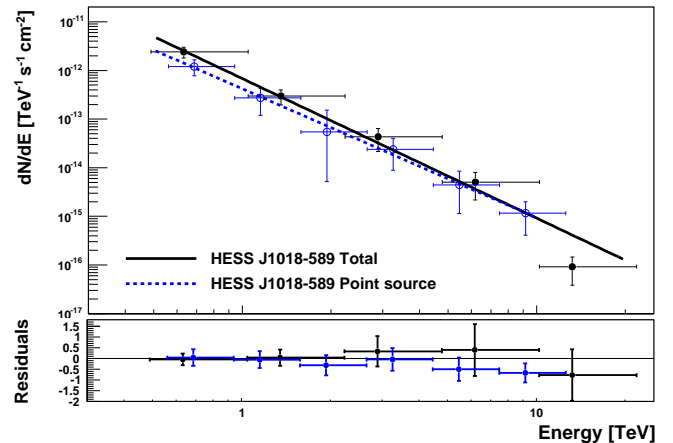


**Fig. 4.** VHE photon spectrum of HESS J1018–589 for a point-like source at position A (in blue dots and dashed blue line) and derived from a region of size  $0.30^\circ$  comprising the point-like and diffuse emission (in black dots and solid black line.). The residuals to the fit are shown in the bottom panel.

like source and a second region of  $0.30^\circ$  radius accounting for the total VHE  $\gamma$ -ray emission centered on  $\alpha=10^{\text{h}}17^{\text{m}}45.6^{\text{s}}$  and  $\delta=-59^\circ 00' 00''$  (J2000). The photon spectra in both cases are well represented with a simple power-law function  $dN/dE=N_0(E/1\text{ TeV})^{-\Gamma}$ . The point-like source has a photon index of  $\Gamma=2.7\pm 0.5_{\text{stat}}\pm 0.2_{\text{sys}}$  statistically compatible with the total ( $0.30^\circ$ ) VHE  $\gamma$ -ray emission region,  $\Gamma=2.9\pm 0.4_{\text{stat}}\pm 0.2_{\text{sys}}$ . The normalization constants at 1 TeV are  $N_0=(4.2\pm 1.1)\cdot 10^{-13}\text{ TeV}^{-1}\text{ cm}^{-2}\text{ s}^{-1}$  and  $N_0=(6.8\pm 1.6)\cdot 10^{-13}\text{ TeV}^{-1}\text{ cm}^{-2}\text{ s}^{-1}$  for the point-like source and the total emission region, respectively. The systematic error on the normalization constant  $N_0$  is estimated from simulated data to be 20% (Aharonian et al. 2006b).

Finally, Fig. 5 shows the light curve of the point-like emission region, integrated between 0.6 TeV and 10 TeV. The Lomb-Scargle test (Scargle 1982) was applied to the data to search for periodicity or variability without positive results for this data set. Fitting a constant to the integrated flux yields a  $\chi^2/\nu$  of 67.2/66, equivalent to a variable integral flux on a run-by-run basis at the level of  $1.0\sigma$ . The lack of orbital coverage prevents any firm conclusion on variability of the TeV emission at the Fermi-LAT reported period (16.58 days).

### 3. X-ray observations with XMM-Newton

XMM-Newton observations were acquired (ID: 0604700101, PI. E. de Oña Wilhelmi) to investigate the origin of the VHE emission region. The field was observed on the 22<sup>nd</sup> August 2009, with a total integration time of 20ksec. The observations were centered on  $\alpha=10^{\text{h}}18^{\text{m}}55.60^{\text{s}}$  and  $\delta=-58^\circ 55' 56.8''$  (J2000) and acquired with the EPIC-PN (Strüder et al. 2001) and EPIC-MOS (Turner et al. 2001) cameras in full-frame mode with a medium filter in a single pointing. This position allowed a good coverage of the whole SNR structure in the EPIC cameras.

The data were analyzed using the XMM Science Analysis System (SAS v11.0.0<sup>1</sup>) and calibration files valid

<sup>1</sup> <http://xmm.esac.esa.int/sas/>

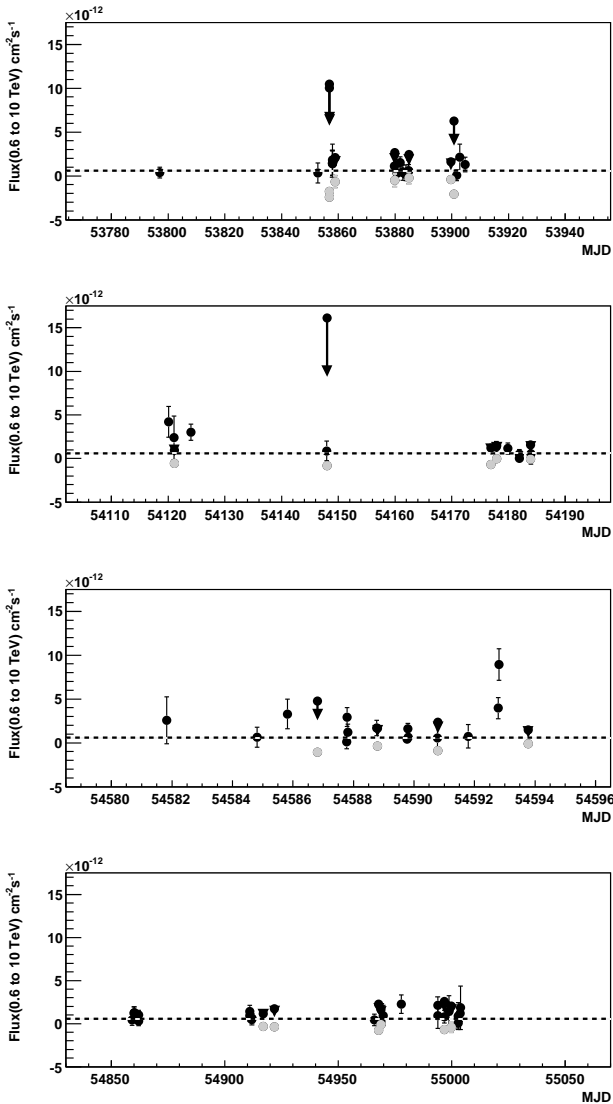


**Fig. 5.** Light curve of the integral flux between 0.6 TeV and 10 TeV in a  $0.1^\circ$  region centered on position A binned such that each point represents the data in one H.E.S.S. observing run (typically 28 min). An upper limit for 99% confidence level is shown with an arrow when the fluctuation in the integral flux is negative (grey points). The dashed horizontal line shows the mean integral flux.

at September 2011. To exclude high background flares, which could potentially affect the observations, light curves were extracted above 10 keV for the entire FoV of the EPIC cameras, but no contamination was found. Therefore the full data set was used for the image and spectral analysis. To create images, spectra, and light curves, events with FLAG=0, and PATTERN=12 (MOS) and 4 (PN) were selected. Hereafter clean event files in the 0.3 to 8 keV energy band are used.

Images combining the different EPIC instruments (see Fig. 6 a) and b)), vignetting-corrected and subtracted for particle induced and soft proton background, were produced using the *ESAS* analysis package (integrated in SAS). In the 0.3 keV to 2 keV energy range a bright source is detected (see Fig. 6 a)). The radial profile of this central source was derived from the three EPIC cameras and fit

with the corresponding PSF, confirming its point-like nature within the instrument angular resolution and observation sensitivity. This source is surrounded by diffuse emission extending up to the radio shell. A strong enhancement of the diffuse emission is visible just downstream of the radio and H $\alpha$  filament (see Fig. 6 a) and d)). At higher energies (2 to 8 keV, see Fig. 6 b)), the diffuse emission is strongly suppressed suggesting a thermal nature of the emission pervading the SNR, the only significant feature being the bright point-like central source.

This source, dubbed XMMU J101855.4–58564, is located at  $\alpha=10^{\text{h}}18^{\text{m}}55.40^{\text{s}}$  and  $\delta=-58^\circ56'45.6''$  (J2000) with statistical error of  $\pm 0.25''$  in each coordinate (derived using the SAS task *edetect*). The position is compatible with the one derived by Pavlov et al. (2011) The photon spectrum of the point-like source was derived integrating over a  $20''$  circle around the fit position and the background was estimated from a circle of  $40''$  located in the vicinity. The spectrum is well fit ( $\chi_{\text{red}}^2=0.97$ ,  $\nu=159$ ) by an absorbed power-law function in the 0.5 to 7.5 keV energy range, with a photon index of  $\Gamma_x=1.66\pm 0.11_{\text{stat}}$  and an integrated flux of  $F_{2-10\text{keV}}=(6.5\pm 0.7_{\text{stat}})\cdot 10^{-13}\text{ erg cm}^{-2}\text{ s}^{-1}$ . The absorption column density  $N_{\text{H}}$  is  $(6.6\pm 0.8_{\text{stat}})\cdot 10^{21}\text{ cm}^{-2}$ , supporting a Galactic origin of the source. Other models such as a black-body model give fits that are statistically inadequate. Fig. 7 shows the measured spectrum for MOS1, MOS2 and PN (in black, red and green respectively).

Archival 2MASS (Two Micron All Sky Survey) data of the region show a bright star (with magnitudes  $J=10.44\pm 0.02$ ,  $H=10.14\pm 0.02$  and  $K=10.02\pm 0.02$ ) dubbed 2MASS 10185560–5856459, located at  $\alpha=10^{\text{h}}18^{\text{m}}55.6^{\text{s}}$  and  $\delta=-58^\circ56'46''$  (J2000),  $1.3''$  away from XMMU J101855.4–58564, the likely counterpart in the binary system. This source also appears in the USNO<sup>2</sup> catalog with magnitudes  $B=12.76$  and  $R=11.16$ . A distance of  $d_*=5.4_{-2.1}^{+4.6}\text{ kpc}$  to the 2MASS star has been estimated through photometry by Napoli et al. (2011). The position of XMMU J101855.4–58564 is also in agreement with the variable compact object detected by Swift XRT at  $\alpha=10^{\text{h}}18^{\text{m}}55.54^{\text{s}}$  and  $\delta=-58^\circ56'45.9''$  (J2000) and the Fermi-LAT source 1FGL J1018.6–5856 (Corbet et al. 2011).

To the North-East of XMMU J101855.4–58564 a faint extended emission region located just downstream of the radio and H $\alpha$  filament of the remnant is visible at low energy ( $E<2\text{keV}$ ) (Fig. 6 a) and d)). To extract the X-ray spectrum, the background was modeled using the *ESAS* software following the approach of Snowden et al. (2004). This background model is subsequently used to fit the signal region. The final shell spectrum is well represented by an absorbed non-equilibrium ionization (PSHOCK) thermal model with a temperature of  $kT\approx 0.5\text{ keV}$  and a column density of  $8\cdot 10^{21}\text{ cm}^{-2}$  (in Fig. 8). The normalization factor  $A$ , defined as

$$A(\text{cm}^{-5}) = 10^{-14} \int n_e^2 dV / 4\pi d^2 \quad (1)$$

is  $1.5\cdot 10^{-3}\text{ cm}^{-5}$ . From this value, assuming a spherical volume ( $V$ ) corresponding to the  $2'$  source extraction region (see Fig. 6a)) and a fully ionized gas ( $n_e=1.2\cdot n$ ), a plasma density can be derived to be  $n\approx 0.5\text{ cm}^{-3}(2.9\text{ kpc}/d)^2$ .

<sup>2</sup> <http://www.usno.navy.mil/USNO/>

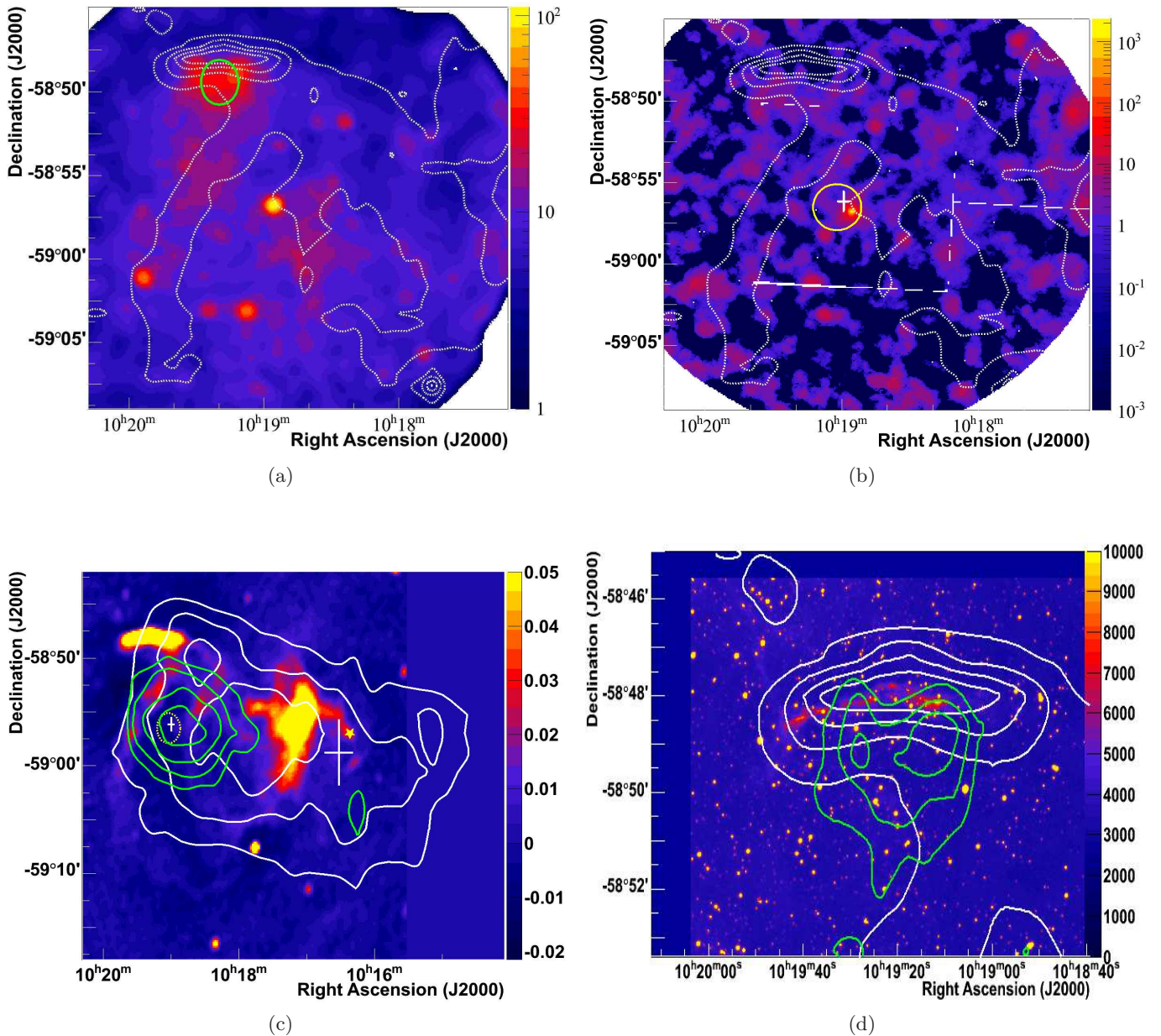


**Fig. 6.** Multi-wavelength view of the HESS J1018–589 region. On the top left a) XMM-*Newton* exposure-corrected counts map centered on SNR G284.3–1.8 in the 0.3 to 2 keV energy band in color scale combining the three EPIC cameras. The image (in excess per arcmin<sup>2</sup>) is in logarithmic scale and it was adaptively smoothed to emphasize the extended thermal emission. The white-dashed contours show the radio image of SNR G284.3–1.8 from MOST-Molonglo observations at 843 MHz. The extraction region to evaluate the diffuse X-ray emission is shown in green. On the top right b) XMM-*Newton* exposure-corrected counts map with the EPIC cameras at high energies in the 2 to 8 keV energy band. The white cross and yellow circle mark the best fit position of the H.E.S.S. point-like emission and the 95% confidence level of the Fermi-LAT source 2FGL J1019.0–5856. On the left bottom c) The significance contours for the two different oversampling radii for HESS J1018–589 are shown in green (0.1°) and white (0.22°). The best-fit positions (white cross) of the VHE  $\gamma$ -ray, superimposed on the MOST-Molonglo radio map are displayed, together with the position of PSR J1016–5857 (yellow star) and 2FGL J1019.0–5856 (in dashed-yellow). On the right bottom d) A zoom of the radio shell (in white) is shown together with the contours of the thermal emission in green and H $\alpha$  observations from the SuperCOSMOS H-alpha Survey (in intensity units).

#### 4. Discussion

A new VHE  $\gamma$ -ray source, HESS J1018–589, has been discovered in the vicinity of the shell-like remnant

SNR G284.3–1.8. The extended TeV emission region coincides with SNR G284.3–1.8 and PSR J1016–5857, both viable candidates to explain the observed VHE  $\gamma$ -ray emission. This emission region is also positionally compatible

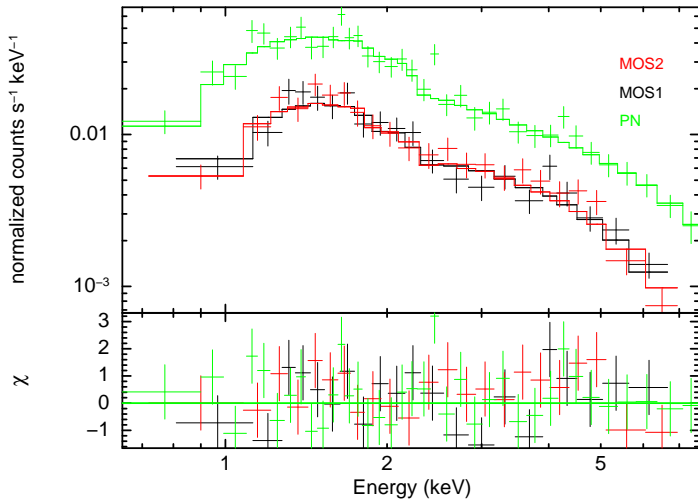


**Fig. 7.** XMM-*Newton*/PN/MOS spectrum of the point-like source XMMU J101855.4–58564, fit with an absorbed power-law model in the 0.5 to 7.5 keV energy range. The bottom panel shows the residuals to the fitted spectra.

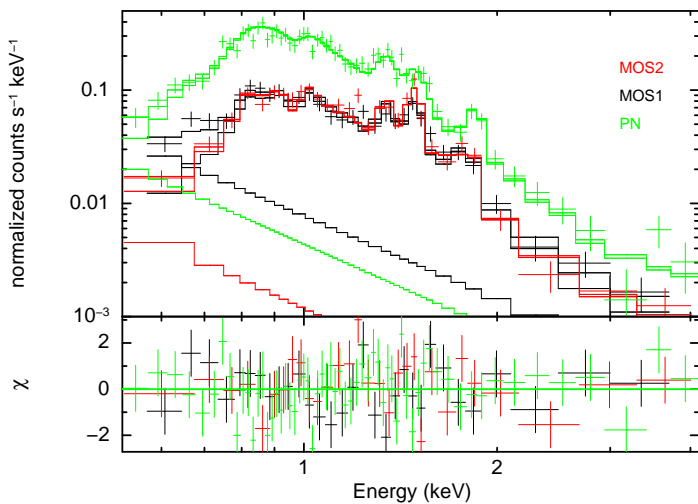


**Fig. 8.** XMM-*Newton*/PN/MOS spectrum of the extended emission region (in green in Fig. 6 a)) fit with an absorbed non-equilibrium ionization (PSHOCK) thermal model. The bottom panel shows the residuals to the fitted spectra.

with the new HE  $\gamma$ -ray binary 1FGL J1018.6–5856 reported recently by the Fermi-LAT collaboration (Corbet et al. 2011). Different possible scenarios in the context of multi-wavelength observations, including new results derived from XMM-*Newton* observations, are discussed in the following.

Although the spectral characteristics and light curve of the H.E.S.S. source do not yet allow a firm identification of the origin of the VHE  $\gamma$ -ray emission, the morphology of the source is considered to clarify the situation. Two distinct emission regions are detected in the H.E.S.S. data, one point-like emission region (A) located in the center of SNR G284.3–1.8 with a centroid compatible with the 95% confidence contour of 1FGL J1018.6–5856, and a diffuse emission region (B) extending towards the direction of PSR J1016–5857, with its centroid compatible with the position of the pulsar.

The new HE  $\gamma$ -ray binary 1FGL J1018.6–5856 shares many characteristics with the VHE  $\gamma$ -ray binary LS 5039 (Aharonian et al. 2005a). The XMM-*Newton* observations presented here reveal a bright non-thermal point-like source, XMMU J101855.4–58564, in the center of the SNR and compatible with the position of the binary system and the H.E.S.S. point-like emission. The X-ray photon spectrum resembles that of pulsars, with a photon spectral index of 1.67 and a column density of  $(6.6 \pm 0.8) \cdot 10^{21} \text{ cm}^{-2}$ , compatible with that from the thermal emission region coincident with the bright radio filament ( $7.9 \cdot 10^{21} \text{ cm}^{-2}$ ). The position of XMMU J101855.4–58564 centered on the SNR and the similar distance (also compatible with the distance to the associated 2MASS star) suggest a physical association between the two objects (rather than an association between the SNR and PSR J1016–5857), namely that the compact object within the binary system was the stellar progenitor for the type II SN explosion (see e. g. Bosch-Ramon & Barkov 2011). No extended emission or putative PWN around the point-like source is observed in the present data at the level of the XMM-*Newton* observation sensitivity. The light curve of the X-ray emission does not show any indication of variability or periodicity on short time scales, for the time resolution of the MOS and PN cameras in full-frame mode (2.6 s and 73.4 ms respectively). XMMU J101855.4–58564 has been associated (Pavlov et al. 2011) with the Swift XRT source, which itself has been identified as a counterpart to the HE binary system. The best-fit position of HESS J1018–589 is compatible within less than  $1\sigma$  with both the position of XMMU J101855.4–58564 and the variable HE source, whose position has been determined accurately using timing analysis. The spectral type of the possible companion star, O6V((f)) is similar to the one in the VHE  $\gamma$ -ray binary LS 5039.

In a binary scenario composed of a massive star and a pulsar or a black hole, modulated VHE  $\gamma$ -rays can be produced by different mechanisms, namely inverse Compton emission or pions produced by high-energy protons interacting with the stellar wind (Bednarek 2006; Dubus 2006; Khangulyan et al. 2008; Kirk et al. 1999; Sierpowska-Bartosik & Torres 2008). Similar to previously detected VHE binary systems such as LS 5039, LSI +61 303 (Albert et al. 2009) and PSR B1259–63 (Aharonian et al. 2005b) periodic emission is found at HE. Despite the similarities with other VHE binaries and in particular LS 5039, and the good positional agreement with the Fermi-LAT source, the association of the H.E.S.S. source (A) with 1FGL J1018.6–5856 is still uncertain. No flux variability has been observed yet and the Lomb-Scargle test does not recover the Fermi-LAT reported 16.58 days modulation of the HE signal. Nevertheless it should be noted that the non-detection might be due to possible contamination from the neighboring diffuse emission, statistics of the data set, and inadequate time sampling of the orbit.

HESS J1018–589 (A) is also coincident with the SNR G284.3–1.8. SNRs are believed to be sites of particle acceleration up to at least a few tens of TeV. Two types of VHE  $\gamma$ -ray emission associated with SNRs have been discovered with IACTs, VHE  $\gamma$ -ray emission from shell-like SNRs such as RX J1713.7–3947 (Aharonian et al. 2007) or SN 1006 (Acero et al. 2010), in which in general the VHE morphology is in good agreement with the synchrotron X-ray emission; and VHE  $\gamma$ -ray radiation which seems to originate through proton-proton (p-p) interaction of cos-

mic rays (CR) accelerated in the SNR interacting with local MCs in the vicinity, such as W28 (Aharonian et al. 2008b). Ruiz & May (1986) reported evidence of interaction of SNR G284.3–1.8 with embedded MC, constraining the distance to the SNR to  $\approx 2.9$  kpc. The analysis performed in the context of this work of public  $^{12}\text{CO}$  ( $J=1-0$ ) data from the CfA 1.2 m Millimeter-Wave Telescope (Dame et al. 2001) yields an estimate of the MC mass of  $\approx 3 \cdot 10^3 M_{\odot}$ . Ruiz & May (1986) also reported on optical observations in the direction of SNR G284.3–1.8 and associated a bright optical filament (Fig. 6 d)) coincident with the brightest shell structure to the North-East, indicating collisional excitation of the ISM, swept by the expanding SNR shock wave. The observed MCs, if indeed physically associated with the SNR, could provide enough target material to explain the VHE emission in a scenario in which the  $\gamma$ -ray are produced via p-p interaction. However, contrary to some other SNRs at VHE, the emission detected with H.E.S.S. does not match the shell-type morphology within the present statistics.

The diffuse emission detected with H.E.S.S. (B) extends towards the direction of PSR J1016–5857. PSR J1016–5857 was detected as a bright EGRET source and pulsed emission at HE has been reported by the AGILE (Pellizzoni et al. 2009) and the Fermi-LAT (Saz Parkinson et al. 2010) collaborations. With a spin-down luminosity of  $2.6 \cdot 10^{36} \text{ ergs}^{-1}$ , the radio, HE and X-ray pulsar PSR J1016–5857 is energetic enough to power the entire H.E.S.S. source, assuming a dispersion-measured estimated distance of 9 kpc. In this scenario, particles are accelerated in the wind termination shock and produce VHE  $\gamma$ -ray emission by inverse Compton (IC) processes as they propagate away from the pulsar. As a result of the interactions of relativistic leptons with the local magnetic field and low-energy radiation, non-thermal radiation is produced up to  $\approx 100$  TeV (for a recent review see de Jager & Djannati-Ataï 2008). Assuming a distance of 9 kpc, the total VHE luminosity in the 1 to 10 TeV energy range is  $9.7 \cdot 10^{33} \cdot (d/9 \text{ kpc})^2 \text{ ergs}^{-1}$ , implying a maximum conversion from rotational energy into non-thermal emission with efficiency 0.4%, with similar features to other well-established VHE PWNe, such as Vela X (Aharonian et al. 2006d) or HESS J1026–582 (Abramowski et al. 2010). The associated X-ray nebula has been detected with Chandra in the 0.8 to 7 keV energy range with a size of  $3'$ . The different size of the VHE and X-ray nebula,  $\approx 20 \cdot (d/9 \text{ kpc}) \text{ pc}$  and  $\approx 8 \cdot (d/9 \text{ kpc}) \text{ pc}$  respectively, can be easily accommodated in a relic nebula scenario, and explained by the different energies (and hence cooling times) of the electron population emitting X-rays and VHE  $\gamma$ -rays as seen, e. g. in HESS J1825–137 (Aharonian et al. 2006a) for a low magnetic field of the order of a few  $\mu\text{G}$ .

## 5. Conclusions

A new VHE  $\gamma$ -ray source dubbed HESS J1018–589 has been detected with the H.E.S.S. telescope array with a significance of  $8.3\sigma$ . The complex VHE morphology and faint VHE emission prevent a unequivocal identification of the source given the presence of several possible counterparts. The H.E.S.S. source seems to be composed of two emission regions but the statistics are still too low to make firm conclusions about the origin of those.

Several counterparts are discussed using energetics arguments as to the possible origin of either part or all of the emission. In a SNR/MC scenario, SNR G284.3–1.8 could partially explain the VHE  $\gamma$ -ray emission via p-p interactions with the associated MCs. However the fact that the VHE emission does not trace either the irregular shell or the cloud morphology disfavors SNR G284.3–1.8 as the only counterpart.

The morphology and good positional agreement between the H.E.S.S. best-fit position A and the new Fermi-LAT binary 1FGL J1018.6–5856 suggest a common origin. The analysis of the XMM-*Newton* observations revealed a non-thermal point-like source, XMMU J101855.4–58564, with photon spectral index of 1.67, similar to the compact object found in LS 5039. Likewise, the spectral class of the massive star companion listed in the 2MASS and USNO catalogs is similar to the one in LS 5039. However, no variability has been found in the H.E.S.S. light curve. A dedicated observation campaign at VHE should help to clarify whether or not the two sources are indeed associated.

The energetic pulsar PSR J1016–5857, also recently detected in Fermi-LAT and AGILE data, and its X-ray nebula seem the most likely candidate to power the extended VHE  $\gamma$ -ray source, given the high spin-down luminosity ( $2.6 \cdot 10^{36} \text{ ergs}^{-1}$ ) and X-ray nebula, which implies a population of high energy electrons able to up-scatter soft photon fields to VHE. The estimated age of the pulsar (21 kyr) would also explain the large size of the VHE nebula, similar to other systems such as Vela X (Aharonian et al. 2006d).

Finally, XMM-*Newton* observations also revealed thermal emission behind the brightest synchrotron part of the radio shell of SNR G284.3–1.8, which might be associated with shock heated interstellar matter. The column density is statistically compatible with the one derived from the direction of XMMU J101855.4–58564. The similar column density and the position of the pulsar candidate with respect to the center of the SNR could indicate a common origin, where XMMU J101855.4–58564 is interpreted as the pulsar left behind after the supernova explosion.

*Acknowledgements.* The support of the Namibian authorities and of the University of Namibia in facilitating the construction and operation of H.E.S.S. is gratefully acknowledged, as is the support by the German Ministry for Education and Research (BMBF), the Max Planck Society, the French Ministry for Research, the CNRS-IN2P3 and the Astroparticle Interdisciplinary Programme of the CNRS, the U.K. Science and Technology Facilities Council (STFC), the IPNP of the Charles University, the Polish Ministry of Science and Higher Education, the South African Department of Science and Technology and National Research Foundation, and by the University of Namibia. We appreciate the excellent work of the technical support staff in Berlin, Durham, Hamburg, Heidelberg, Palaiseau, Paris, Saclay, and in Namibia in the construction and operation of the equipment. This research has made use of the NASA/IPAC Infrared Science Archive, which is operated by the Jet Propulsion Laboratory, California Institute of Technology, under contract with the National Aeronautics and Space Administration.

## References

- Ackermann, M. et al. (Fermi Collaboration) 2012, *Science*, 335, 189.
- Abdo, A. et al. (Fermi Collaboration) 2011, submitted to *ApJS*, arXiv:1108.1435v1.
- Abdo, A. et al. (Fermi Collaboration) 2010, *ApJS*, 188, 405.
- Abramowski, A. et al. (H.E.S.S. Collaboration) 2010, *A&A*, 525, 46.



- Acero, F. et al. (H.E.S.S. Collaboration) 2010 *A&A*, 516, A62.
- Acero, F. et al. (H.E.S.S. Collaboration) 2009, *Science*, 326, 5956, 1080.
- Aharonian, F. A. et al. (H.E.S.S. Collaboration) 2008a, *A&A*, 477, 353.
- Aharonian, F. A. et al. (H.E.S.S. Collaboration) 2008b, *A&A*, 481, 401.
- Aharonian, F. A. et al. (H.E.S.S. Collaboration) 2007, *A&A*, 464, 235.
- Aharonian, F. A. et al. (H.E.S.S. Collaboration) 2006a, *A&A*, 460, 365.
- Aharonian, F. A. et al. (H.E.S.S. Collaboration) 2006b, *A&A*, 457, 899.
- Aharonian, F. A. et al. (H.E.S.S. Collaboration) 2006c, *ApJ*, 636, 777.
- Aharonian, F. A. et al. (H.E.S.S. Collaboration) 2006d, *A&A*, 448, 43.
- Aharonian, F. A. et al. (H.E.S.S. Collaboration) 2005a, *Science* 309, 746.
- Aharonian, F. A. et al. (H.E.S.S. Collaboration) 2005b, *A&A*, 442,1.
- Albert, J. et al. (MAGIC Collaboration) 2009, *ApJ*, 693, 303.
- Becherini, Y. et al. 2011, *Astroparticle Phys.*, 34, 858.
- Bednarek, W. 2006, *MNRAS* 368, 579.
- Bell, A. R. 1978, *MNRAS*, 182, 147.
- Bosch-Ramon, V. & Barkov, M. V., 2011, *A&A*, in press, arXiv:astro-ph/1105.6236v1.
- Camilo, F. et al. 2001, *ApJ*, 557, 51.
- Camilo, F. et al. 2004, *ApJ*, 616, 1118.
- Corbet, R. H. D. et al. (Fermi Collaboration) 2011, *ATel* #3221.
- Cordes, J. M. & Lazio, T. J. W. 2002, arXiv:astro-ph/0207156.
- Dame, T. M., Hartmann, D. & Thaddeus, P. 2001, *ApJ*, 547, 792.
- Dubus, G. 2006, *A&A*, 451, 9.
- de Jager, O.C & Djannati-Ataï, A. 2008, *Astrophys. & Space Sci.*, 67, 357.
- Funk, S., Hermann, G., Hinton, J. et al. 2004, *Astroparticle Phys.*, 22, 285.
- Gast, H. et al. (H.E.S.S. Collaboration) 2011, in *Proceedings of the 22th International Cosmic Ray Conference*, Beijing.
- Gillessen, S. 2004, Ph.D. thesis, University of Heidelberg.
- Hartman, R. C. et al. 1999, *ApJS*, 123, 79.
- Hillas, A. M., 1984, in *Proceedings of the 19th International Cosmic Ray Conference*, La Jolla edited by Frank C. Jones et al. (NASA, Washington, D.C.).
- Khangulyan, D., Aharonian F. & Bosch-Ramon, V. 2008, *MNRAS*, 383, 467.
- Kirk, J. G., Ball, L., & Skjaeraasen, O. 1999, *Astroparticle Phys.* 10, 31.
- Li, J. et al. 2011, Accepted for publication in *ApJ Letters*, arXiv:astro-ph/1108.1668v1.
- Milne, D. K. et al., 1989, *Proc. ASA* 8, 2.
- Napoli, V. J. et al., 2011, *PASP*, in press, arXiv:astro-ph/1109.3692v1.
- de Naurois, M. & Rolland, L. 2009, *Astroparticle Phys.* 32, 231.
- Pavlov, G. G. et al. 2011, *ATel* #3228.
- Pellizzonni, A. et al. (AGILE Collaboration) 2009, *ApJ* 695, L115.
- Piron, F., Djannati-Ataï, A., Punch, M. et al. 2001, *A&A* 374, 895.
- Refsdal, B., Doe, S., Nguyen, D., et al. 2009, *Proceedings of the 8th Python in Science conference (SciPy 2009)* G. Varoquaux, S. van der Walt, J. Millman (Eds.) 51.
- Ruiz, M. T. & May, J. 1986, *ApJ*, 309, 667.
- Saz Parkinson, P. M. (Fermi Collaboration) (2011) *Proceed. of Pulsar Conference*, Sardinia, to be published by AIP.
- Scargle, J. D. 1982, *ApJ*, 263, 835.
- Sierpowska-Bartosik, A. & Torres, D. F. 2008, *ApJ* 30, 239.
- Snowden, S. L., Collier, M. R. & Kuntz, K. D. 2004, *ApJ*, 610, 1182.
- Strüder, L. et al., 2001 *A&A*, 365, L18.
- Taylor, J. H., & Cordes, J. M. 1993, *ApJ*, 411, 674.
- Turner, M. J. L. et al. 2001, *A&A*, 365, L27.
- Van der Bergh, S., Marscher, A. P. & Terzian, Y. 1973, *ApJ*, 239, 873.
- 
- <sup>1</sup> Universität Hamburg, Institut für Experimentalphysik, Luruper Chaussee 149, D 22761 Hamburg, Germany
- <sup>2</sup> Laboratoire Univers et Particules de Montpellier, Université Montpellier 2, CNRS/IN2P3, CC 72, Place Eugène Bataillon, F-34095 Montpellier Cedex 5, France
- <sup>3</sup> Max-Planck-Institut für Kernphysik, P.O. Box 103980, D 69029 Heidelberg, Germany
- <sup>4</sup> Dublin Institute for Advanced Studies, 31 Fitzwilliam Place, Dublin 2, Ireland
- <sup>5</sup> National Academy of Sciences of the Republic of Armenia, Yerevan
- <sup>6</sup> Yerevan Physics Institute, 2 Alikhanian Brothers St., 375036 Yerevan, Armenia
- <sup>7</sup> Universität Erlangen-Nürnberg, Physikalisches Institut, Erwin-Rommel-Str. 1, D 91058 Erlangen, Germany
- <sup>8</sup> Nicolaus Copernicus Astronomical Center, ul. Bartycka 18, 00-716 Warsaw, Poland
- <sup>9</sup> CEA Saclay, DSM/IRFU, F-91191 Gif-Sur-Yvette Cedex, France
- <sup>10</sup> Astroparticule et Cosmologie (APC), CNRS, Université Paris 7 Denis Diderot, 10, rue Alice Domon et Léonie Duquet, F-75205 Paris Cedex 13, France (UMR 7164: CNRS, Université Paris VII, CEA, Observatoire de Paris)
- <sup>11</sup> Laboratoire Leprince-Ringuet, Ecole Polytechnique, CNRS/IN2P3, F-91128 Palaiseau, France
- <sup>12</sup> Institut für Theoretische Physik, Lehrstuhl IV: Weltraum und Astrophysik, Ruhr-Universität Bochum, D 44780 Bochum, Germany
- <sup>13</sup> Institut für Physik, Humboldt-Universität zu Berlin, Newtonstr. 15, D 12489 Berlin, Germany
- <sup>14</sup> LUTH, Observatoire de Paris, CNRS, Université Paris Diderot, 5 Place Jules Janssen, 92190 Meudon, France
- <sup>15</sup> LPNHE, Université Pierre et Marie Curie Paris 6, Université Denis Diderot Paris 7, CNRS/IN2P3, 4 Place Jussieu, F-75252, Paris Cedex 5, France
- <sup>16</sup> Institut für Astronomie und Astrophysik, Universität Tübingen, Sand 1, D 72076 Tübingen, Germany
- <sup>17</sup> Astronomical Observatory, The University of Warsaw, Al. Ujazdowskie 4, 00-478 Warsaw, Poland
- <sup>18</sup> Unit for Space Physics, North-West University, Potchefstroom 2520, South Africa
- <sup>19</sup> University of Durham, Department of Physics, South Road, Durham DH1 3LE, U.K.
- <sup>20</sup> Landessternwarte, Universität Heidelberg, Königstuhl, D 69117 Heidelberg, Germany
- <sup>21</sup> Oskar Klein Centre, Department of Physics, Stockholm University, Albanova University Center, SE-10691 Stockholm, Sweden
- <sup>22</sup> University of Namibia, Department of Physics, Private Bag 13301, Windhoek, Namibia

<sup>23</sup> Laboratoire d’Astrophysique de Grenoble, INSU/CNRS, Université Joseph Fourier, BP 53, F-38041 Grenoble Cedex 9, France

<sup>24</sup> Department of Physics and Astronomy, The University of Leicester, University Road, Leicester, LE1 7RH, United Kingdom

<sup>25</sup> Instytut Fizyki Jądrowej PAN, ul. Radzikowskiego 152, 31-342 Kraków, Poland

<sup>26</sup> Institut für Astro- und Teilchenphysik, Leopold-Franzens-Universität Innsbruck, A-6020 Innsbruck, Austria

<sup>27</sup> Laboratoire d’Annecy-le-Vieux de Physique des Particules, Université de Savoie, CNRS/IN2P3, F-74941 Annecy-le-Vieux, France

<sup>28</sup> Obserwatorium Astronomiczne, Uniwersytet Jagielloński, ul. Orła 171, 30-244 Kraków, Poland

<sup>29</sup> Toruń Centre for Astronomy, Nicolaus Copernicus University, ul. Gagarina 11, 87-100 Toruń, Poland

<sup>30</sup> School of Chemistry & Physics, University of Adelaide, Adelaide 5005, Australia

<sup>31</sup> Charles University, Faculty of Mathematics and Physics, Institute of Particle and Nuclear Physics, V Holešovičkách 2, 180 00 Prague 8, Czech Republic

<sup>32</sup> School of Physics & Astronomy, University of Leeds, Leeds LS2 9JT, UK

<sup>33</sup> European Associated Laboratory for Gamma-Ray Astronomy, jointly supported by CNRS and MPG